

# CGC-induced longitudinal ridge in p-Pb collisions

Donghai Zhang,<sup>1,\*</sup> Yeyin Zhao,<sup>2</sup> Luhua Qiu,<sup>3</sup> Mingmei Xu,<sup>3,†</sup> and Yuanfang Wu<sup>3,‡</sup>

<sup>1</sup>*School of Physics and Astronomy, China West Normal University, Nanchong 637002, China*

<sup>2</sup>*School of Physics and Electronic Engineering, Sichuan University of Science and Engineering, Zigong 643000, China*

<sup>3</sup>*Key Laboratory of Quark and Lepton Physics (MOE) and Institute of Particle Physics, Central China Normal University, Wuhan 430079, China*

Within the Color Glass Condensate (CGC) effective field theory, we investigate the long-range rapidity correlations in proton-lead (p-Pb) collisions at  $\sqrt{s_{\text{NN}}} = 5.02$  TeV. As expected, the long-range rapidity correlations rebound after bottoming, which is successfully reproduced by the CGC. It is also found that the correlation rebound appears around the sum of the saturation momenta of the projectile and target, and moves to larger rapidities at higher collision energies. Beyond that, the longitudinal rapidity correlations are asymmetrically distributed in p-Pb collisions when the transverse momenta of two particles differ, while become symmetric when the transverse momenta of two particles coincide. This feature of rapidity correlations is unique to asymmetric pA collisions, and directly results from the saturation and the quantum evolution of gluons within the framework of the CGC.

## I. INTRODUCTION

Two-particle correlations are a powerful tool to explore the mechanism of particle production in hadrons and nucleus collisions at high energy. Such studies involve measuring the distributions of relative azimuthal angle  $\Delta\phi$  and relative pseudorapidity  $\Delta\eta$  between pairs of particles. The  $\Delta\eta$ - $\Delta\phi$  correlation functions for photonuclear ( $\gamma$ A) collisions [1], proton-proton (pp) [2–7], proton-nucleus (pA) [8–13] and nucleus-nucleus (AA) collisions [14–19], show similar structures. An enhancement is observed on the near side (relative azimuthal angle  $\Delta\phi \approx 0$ ), which extends over a broad range in relative pseudorapidity ( $|\Delta\eta| \approx 4$ ). Specifically, a rebound at  $|\Delta\eta| \approx 4$  after a plateau within  $2 < |\Delta\eta| < 3.6$  is observed [3]. Such a long-range correlation of the near side is often referred to as the “ridge”. Ridge structure was first observed in relativistic AA collisions and is widely regarded as a product of the collective dynamics of quark-gluon plasma (QGP) [20–26]. Later, similar phenomena were observed in high-multiplicity pA and pp collisions, even in  $\gamma$ A collisions, which has aroused new discussions on the origin of the collectivity in small systems.

The origin of ridge correlations in high-energy small system collisions has sparked intense debate between two competing mechanisms. One is the CGC effective field theory based on initial-state intrinsic momentum anisotropy [27–35], and the other is final-state interaction of collective response to the collision geometry described by hydrodynamics [36–40].

The hydrodynamic model, using fluid evolution and various initial conditions, gives a systematical description of the ridge phenomenon in small systems and heavy-ion collisions [41, 42]. Several other observations, like

mass-ordering of the elliptic flow coefficient ( $v_2$ ) of identified particles [44], quark-number scaling of  $v_2$  [45] and baryon-to-meson enhancement at intermediate  $p_T$  [46] suggest similarity in small systems and heavy-ion collisions. However, the model fails to reproduce multiple-particle cumulant  $c_2\{4\}$  [43]. Moreover, the absence of significant jet-quenching indicates that the QGP medium may be transparent to the small systems [47, 48], in which case hydrodynamics may not be applicable.

On the other hand, CGC successfully explained the mass ordering of  $v_2$  [49], multiple-particle cumulant  $c_2\{4\}$  [50], and the elliptic flow of  $\gamma$ A process [35], except the ordering of Fourier harmonics  $v_n$  in the three system sizes of p-Au, d-Au and He-Au [51]. Furthermore, sizable signals of collectivity have been found not only for soft and light hadrons but also for heavy flavor mesons [52–55] in small systems. In this respect, CGC successfully explained experimental data [56], hydrodynamics failed [57]. In brief, either hydrodynamics or CGC might not rule data all. Recent research [58–60] shows that the azimuthal anisotropy measured in small systems may result from the coexistence of CGC and hydrodynamics.

The gluon density inside hadron or nucleus sharply grows at small Bjorken  $x$  or high energy. The framework to describe the physics of high parton densities and gluon saturation inside projectile and target hadron or nucleus is the CGC effective field theory [61]. The effective degrees of freedom in this framework are color sources  $\rho$  at large  $x$  and gauge fields  $\mathcal{A}_\mu$  at small  $x$ . The classical gauge field  $\mathcal{A}_\mu$  is the solution of classical Yang-Mills equations with a fixed configuration of color sources. Its dynamical evolution is captured by the Balitsky-Kovchegov equation with running coupling kernel [62–64]. The quantum evolution of projectiles [28] starts from the radiations of valence quarks and produces gluons. Successive gluon splittings produce more gluons. Gluon recombination stops the increase of the gluon density. Ultimately, these processes lead to gluon saturation inside projectile.

\*Electronic address: zdh@cwnu.edu.cn

†Electronic address: xumm@cnu.edu.cn

‡Electronic address: wuyf@cnu.edu.cn

The projectile and target hadron or nucleus of high gluon density are two sheets of strongly correlated coherent gluonic fields, which is called color glass condensate. When two sheets of CGCs shatter in a high-multiplicity collision, the strong longitudinal color electric and color magnetic fields are formed in the colliding region and are called glasma [65]. Particles with large rapidity separation are produced locally in the transverse plane and correlated by approximately boost invariant glasma flux tubes, generated the long-range rapidity correlations.

In high energy limit, the Bjorken  $x$  of a gluon is related to its rapidity  $y$  in the center-of-mass frame and transverse momentum  $p_T$ . The relation reads

$$x = \frac{p_T}{\sqrt{s}} e^{\pm y}, \quad (1)$$

with  $\sqrt{s}$  center-of-mass energy,  $+(-)$  corresponding to the right(left) moving projectile(target). The dependence on rapidity is much more sensitive due to the exponential function. At  $\sqrt{s} = 5.02$  TeV and intermediate  $p_T$ , e.g. 2 GeV/ $c$ , for a right moving projectile, gluons with  $y \gtrsim 3.2$  have  $x > x_0$  ( $x_0 = 0.01$  is starting value of small- $x$  dynamic evolution). They are called source gluons. Gluons with  $y \lesssim 0.9$  and  $x < 0.001$  are descendants of source gluons and are called radiated gluons. In central rapidity region, radiated gluons with small  $x$  in a colliding hadron are probed, while in the large rapidity region, source gluons at large  $x$  are probed. Therefore, the physics in different rapidity regions is different. Correlations of gluons of different rapidity regions essentially reflect correlations of different generations [66–70]. Large-rapidity ridge correlations probe strong correlations between source gluons and radiated gluons.

The experimental observable of ridge is per-trigger yield [3–5, 7–9, 12, 14–16], i.e., the number of particle pairs with pseudo-rapidity interval  $\Delta\eta$  and azimuthal interval  $\Delta\phi$  divided by the number of trigger particles. In order to eliminate the influence of uncorrelated pairs, mixed events are usually constructed in experiments. Dividing the yield in real events by the yield in mixed events gives the final results reported in experiments.

In the CGC calculation, we correct the number of uncorrelated pairs as the integral of the product of two single-particle distributions within the acceptance [70]. Using this correction in p-Pb collisions, the ridge yield at large rapidity rebounds after bottoming, which is successfully reproduced and described by the CGC. The correlation rebound is further found to happen at even larger rapidity region for higher colliding energies, and is most obvious around the sum of the saturation momenta of the projectile and target. These features of the correlation rebound in p-Pb collisions are closely related to the mechanism of CGC.

It is also found that the near-side rapidity correlations are asymmetric in p-Pb collisions when the transverse momenta of two particles differ, but become symmetric when the transverse momenta of two particles coincide. The asymmetry in rapidity correlations stems from the

inherent asymmetry of the colliding hadron or nucleus in rapidity. In the CGC framework, the gluon at different rapidity regions reflects the properties of different  $x$  degree of freedom and corresponds to different stages of gluon evolution. Therefore, the asymmetry in rapidity correlations are sensitive to the quantum evolution of gluon saturation dynamics.

This paper is organized as follows. The definition of correlation function and some related formulae in CGC framework are given in section II. The formulae in this manuscript follow those in Refs. [31–33, 66–70] and are identical with those at gluon level without fragmentation functions. In section III, the per-trigger yield in the  $\Delta y$ - $\Delta\phi$  plane for 5.02 TeV p-Pb collisions is presented. In section IV, the dependence of large-rapidity correlations on transverse momentum is systematically studied and the origin is discussed. Section V is a brief summary and discussions.

## II. TWO-PARTICLE CORRELATIONS IN THE FRAMEWORK OF CGC

The per-trigger yield is defined as

$$Y(\Delta y, \Delta\phi) = \frac{1}{N_{\text{Trig}}} \frac{d^2 N^{\text{pair}}}{d\Delta y d\Delta\phi} = B(0, 0) \frac{S(\Delta y, \Delta\phi)}{B(\Delta y, \Delta\phi)}. \quad (2)$$

It counts the number of particle pairs with rapidity separation  $\Delta y$  and azimuthal angle separation  $\Delta\phi$ , divided by the number of trigger particles.

The functions  $S(\Delta y, \Delta\phi)$  and  $B(\Delta y, \Delta\phi)$  are the per-trigger yield obtained from the original and mixed events, respectively. They are known as the signal and background distributions, denoted as

$$S(\Delta y, \Delta\phi) = \frac{1}{N_{\text{Trig}}} \frac{d^2 N^{\text{same}}}{d\Delta y d\Delta\phi}, \quad (3)$$

$$B(\Delta y, \Delta\phi) = \frac{1}{N_{\text{Trig}}} \frac{d^2 N^{\text{mixed}}}{d\Delta y d\Delta\phi}, \quad (4)$$

respectively.

The per-trigger yield obtained from the original events, i.e., signal distributions  $S(\Delta y, \Delta\phi)$  in Eq. (3), not only contains correlated pairs, but also uncorrelated pairs.

In experiments, the number of uncorrelated pairs is estimated by mixed events. Particles of a mixed event are drawn randomly from different original events. For a large enough number of original events, in a single mixed event, the probability of having two particles from the same original event is close to zero. The particles in a mixed event are almost independent [71].

Detector effects, such as tracking inefficiency and detector acceptance, can also affect the signal distributions. They largely cancel in the  $S(\Delta y, \Delta\phi)/B(\Delta y, \Delta\phi)$  ratio. The factor  $B(0, 0)$  is the value of  $B(\Delta y, \Delta\phi)$  at  $\Delta y = 0$  and  $\Delta\phi = 0$ .

The signal distribution of the per-trigger yield in CGC is expressed [31–33] as

$$S(\Delta y, \Delta\phi) = \frac{1}{N_{\text{Trig}}} \frac{d^2 N_{\text{assoc}}}{d\Delta y d\Delta\phi}, \quad (5)$$

$$\begin{aligned} \frac{d^2 N_{\text{assoc}}}{d\Delta y d\Delta\phi} &= \int_{y^{\min}-y_{\text{shift}}}^{y^{\max}-y_{\text{shift}}} dy_{\text{p}} \int_{y^{\min}-y_{\text{shift}}}^{y^{\max}-y_{\text{shift}}} dy_{\text{q}} \delta(y_{\text{q}} - y_{\text{p}} - \Delta y) \int_0^{2\pi} d\phi_{\text{p}} \int_0^{2\pi} d\phi_{\text{q}} \delta(\phi_{\text{q}} - \phi_{\text{p}} - \Delta\phi) \\ &\times \int_{p_{\text{T}}^{\min}}^{p_{\text{T}}^{\max}} \frac{dp_{\text{T}}^2}{2} \int_{q_{\text{T}}^{\min}}^{q_{\text{T}}^{\max}} \frac{dq_{\text{T}}^2}{2} \frac{dN_2^{\text{corr}}}{d^2 \mathbf{p}_{\text{T}} dy_{\text{p}} d^2 \mathbf{q}_{\text{T}} dy_{\text{q}}}. \end{aligned} \quad (6)$$

The labels “p” and “q” denote the two particles in the pair, conventionally referred to as “trigger” and “associated” particles, respectively.  $y_{\text{shift}} = 0.465$  is the shift in rapidity in the center-of-mass frame towards the lead fragmentation region in asymmetric p-Pb collisions.

The  $\delta$  function is used to restrict the phase space interval to a given  $\Delta y$  and  $\Delta\phi$ . The integrand function  $\frac{dN_2^{\text{corr}}}{d^2 \mathbf{p}_{\text{T}} dy_{\text{p}} d^2 \mathbf{q}_{\text{T}} dy_{\text{q}}}$  is equal to the double-particle production minus the product of two single-particle productions, i.e.,

$$\frac{dN_2^{\text{corr}}}{d^2 \mathbf{p}_{\text{T}} dy_{\text{p}} d^2 \mathbf{q}_{\text{T}} dy_{\text{q}}} = \frac{dN_2}{d^2 \mathbf{p}_{\text{T}} dy_{\text{p}} d^2 \mathbf{q}_{\text{T}} dy_{\text{q}}} - \frac{dN_1}{d^2 \mathbf{p}_{\text{T}} dy_{\text{p}}} \frac{dN_1}{d^2 \mathbf{q}_{\text{T}} dy_{\text{q}}}. \quad (7)$$

The background distribution in Eq. (4) represents the per-trigger yield of uncorrelated pairs. The counterpart in theoretical calculations should be integrals of the product of two single-particle productions, i.e.,

$$B(\Delta y, \Delta\phi) = \frac{1}{N_{\text{Trig}}} \frac{d^2 N_{\text{uncorr}}}{d\Delta y d\Delta\phi}, \quad (8)$$

$$\begin{aligned} \frac{d^2 N_{\text{uncorr}}}{d\Delta y d\Delta\phi} &= \int_{y^{\min}-y_{\text{shift}}}^{y^{\max}-y_{\text{shift}}} dy_{\text{p}} \int_{y^{\min}-y_{\text{shift}}}^{y^{\max}-y_{\text{shift}}} dy_{\text{q}} \delta(y_{\text{q}} - y_{\text{p}} - \Delta y) \int_0^{2\pi} d\phi_{\text{p}} \int_0^{2\pi} d\phi_{\text{q}} \delta(\phi_{\text{q}} - \phi_{\text{p}} - \Delta\phi) \\ &\times \int_{p_{\text{T}}^{\min}}^{p_{\text{T}}^{\max}} \frac{dp_{\text{T}}^2}{2} \int_{q_{\text{T}}^{\min}}^{q_{\text{T}}^{\max}} \frac{dq_{\text{T}}^2}{2} \frac{dN_1}{d^2 \mathbf{p}_{\text{T}} dy_{\text{p}}} \frac{dN_1}{d^2 \mathbf{q}_{\text{T}} dy_{\text{q}}}. \end{aligned} \quad (9)$$

The integration in Eq. (9) depends on the shape of the single-particle distribution and the acceptance. The background distribution is the function of  $\Delta y$  due to the limited rapidity acceptance. To precisely reproduce the ridge structure observed in experiments, we corrected the background distribution by integrating the product of two real single-particle distributions [70].

with

The single-particle inclusive production reads

$$\begin{aligned} \frac{dN_1}{d^2 \mathbf{p}_{\text{T}} dy_{\text{p}}} &= \frac{\alpha_s(\mathbf{p}_{\text{T}}) N_c S_{\perp}}{\pi^4 (N_c^2 - 1)} \frac{1}{\mathbf{p}_{\text{T}}^2} \\ &\times \int \frac{d\mathbf{k}_{\text{T}}^2}{(2\pi)^2} \Phi_A(y_{\text{p}}, \mathbf{k}_{\text{T}}) \Phi_A(y_{\text{p}}, \mathbf{p}_{\text{T}} - \mathbf{k}_{\text{T}}), \end{aligned} \quad (10)$$

and

$$N_{\text{Trig}} = \iint_{\text{Acceptance}} dy d^2\mathbf{p}_T \frac{dN_1}{d^2\mathbf{p}_T dy_p}. \quad (11)$$

$\Phi$  is unintegrated gluon distribution (uGD). It is related to quark-antiquark dipole forward scattering amplitude  $\mathcal{N}$ , in large  $N_c$  limit [28],

$$\begin{aligned} \Phi(x, \mathbf{k}_T) &= \frac{N_c k_T^2}{4\alpha_s} \int d^2\mathbf{r}_\perp e^{i\mathbf{k}_T \cdot \mathbf{r}_\perp} [1 - \mathcal{N}_{\text{ad.}}(\mathbf{r}_\perp, Y)] \\ &= \frac{\pi N_c k_T^2}{2\alpha_s} \int dr_\perp r_\perp J_0(k_T r_\perp) [1 - \mathcal{N}(r_\perp, Y)]^2. \end{aligned} \quad (12)$$

Where  $J_0$  is Bessel function,  $Y = \ln \frac{x_0}{x} = \ln x_0 - \ln x$  is the rapidity interval of produced gluon. The amplitude  $\mathcal{N}$  is obtained by solving the leading order (LO) running coupling Balitsky-Kovchegov (rcBK) equation at a given initial condition [62–64]. Then the double- and single-particle productions are available.

In large- $N_c$  limit, the leading order rcBK equation reads

$$\frac{\partial \mathcal{N}(\mathbf{r}_\perp, x)}{\partial Y} = \int d^2\mathbf{r}_{\perp 1} K^{\text{run}}(\mathbf{r}_\perp, \mathbf{r}_{\perp 1}, \mathbf{r}_{\perp 2}) [\mathcal{N}(\mathbf{r}_{\perp 1}, x) + \mathcal{N}(\mathbf{r}_{\perp 2}, x) - \mathcal{N}(\mathbf{r}_\perp, x) - \mathcal{N}(\mathbf{r}_{\perp 1}, x)\mathcal{N}(\mathbf{r}_{\perp 2}, x)], \quad (13)$$

where  $\mathbf{r}_\perp = \mathbf{r}_{\perp 1} + \mathbf{r}_{\perp 2}$  is the transverse dipole size,  $K^{\text{run}}$  is running coupling kernel. In order to solve the rcBK equation, the Albacete-Armesto-Milhano-Quiroga-Salgado (AAMQS) initial condition and a running coupling kernel, Balitsky's prescription, are employed [72, 73]. They are denoted as

$$\mathcal{N}_{\text{AAMQS}}(r, x_0) = 1 - \exp \left[ -\frac{1}{4} (r^2 Q_s^2(x_0))^\gamma \ln \left( e + \frac{1}{r\Lambda} \right) \right], \quad (14)$$

$$\begin{aligned} K^{\text{run}}(\mathbf{r}_\perp, \mathbf{r}_{\perp 1}, \mathbf{r}_{\perp 2}) &= \frac{N_c \alpha_s(\mathbf{r}_\perp^2)}{2\pi^2} \left[ \frac{1}{\mathbf{r}_{\perp 1}^2} \left( \frac{\alpha_s(\mathbf{r}_{\perp 1}^2)}{\alpha_s(\mathbf{r}_{\perp 2}^2)} - 1 \right) \right. \\ &\quad \left. + \frac{\mathbf{r}_\perp^2}{\mathbf{r}_{\perp 1}^2 \mathbf{r}_{\perp 2}^2} + \frac{1}{\mathbf{r}_{\perp 2}^2} \left( \frac{\alpha_s(\mathbf{r}_{\perp 2}^2)}{\alpha_s(\mathbf{r}_{\perp 1}^2)} - 1 \right) \right], \end{aligned} \quad (15)$$

respectively. The best fit of data requires that the infrared scale  $\Lambda = 0.241$  GeV, the anomalous dimension  $\gamma = 1.119$  and the initial saturation scale  $Q_{\text{sp}}^2(x_0) = 0.168$  GeV<sup>2</sup> for proton,  $Q_{\text{SA}}^2(x_0) = 0.504$  GeV<sup>2</sup> for lead nucleus [72]. These parameters have successfully described proton structure function  $F_2$  vs.  $x$  [72], single-inclusive  $p_T$  spectra [74] and other experimental data [30–33].

Completing the integrals in Eqs. (6) and (9) with the transverse momentum range  $1 \leq p_T(q_T) \leq 3$  GeV/ $c$  and the rapidity range  $-2.865 \leq y_p(y_q) \leq 1.935$ ,  $Y(\Delta y, \Delta\phi)$  is obtained and shown in Fig. 1(a). In this Letter,  $Y_w$  in all figures denotes the rapidity window in the laboratory system, and the positive rapidity points in the p-going direction.

### III. LONG-RANGE RAPIDITY CORRELATIONS

As Fig. 1(a) shows, at the rapidity window of  $[-2.4, 2.4]$  (the CMS acceptance), the per-trigger yield in the  $\Delta y$ - $\Delta\phi$  plane for 5.02 TeV p-Pb collisions is given. It is similar to the results of pp collisions we obtained in the CGC framework (see Fig. 1(d) in Ref. [70]). In contrast, the ridge structure in p-Pb collisions is more prominent. In the  $\Delta\phi$  direction, the per-trigger yield has two peaks of equal height at  $\Delta\phi = 0$  and  $\pi$ . The two peaks are called azimuthal collimation which is intrinsic to glasma dynamics [31–33]. It contributes to the well-known collectivity in small systems.

In the  $\Delta y$  direction, the ridge yield  $Y$  shows first fall and then rise with  $|\Delta y|$ , i.e., a visible rebound after the plateau in the rapidity direction is presented. In order to observe the trend of the ridge yield  $Y$  more clearly, a projection to  $\Delta y$  axis is made and shown in Fig. 1(b). As the red curve shows, the near-side yield as a function of  $\Delta y$  for 5.02 TeV p-Pb collisions presents a rebound at  $|\Delta y| \approx 3.5$  after a plateau within  $2 < |\Delta y| < 3.5$ . The plateau and the rebound in the rapidity direction calculated by CGC in trend agree with the LHC data [10].

The per-trigger yield within the rapidity window of  $[-0.9, 0.9]$  (the ALICE acceptance) is not shown here. Its characteristics are very similar to the results for  $|\Delta y| < 2$  in Fig. 1(a), without the plateau and rebound in the rapidity direction. Previous studies have indicated that glasma graphs exhibit significant short-range rapidity correlations [67]. Consequently, the longitudinal structure of the two-dimensional distributions is less as flat as the ALICE data [9]. Therefore, for the rapidity gap  $|\Delta y| < 2$ , the two-dimensional distributions from the CGC framework are not directly comparable with data.

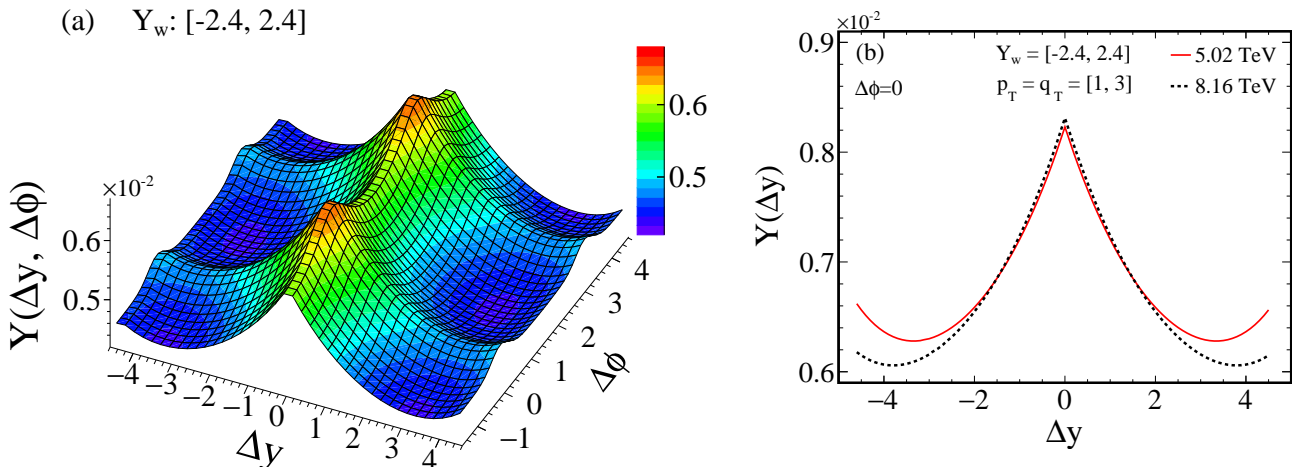


FIG. 1: The per-trigger yield in the  $\Delta y$ - $\Delta\phi$  plane for 5.02 TeV p-Pb collisions with transverse momentum integrated within  $1 \leq p_T(q_T) \leq 3$  GeV/c and with rapidity integrated in  $-2.865 \leq y_p(y_q) \leq 1.935$  (the left panel). The right panel shows the near-side ridge yield projects to  $\Delta y$  axis for p-Pb collisions at 5.02 and 8.16 TeV, respectively.

In order to see how the rebound of long-range rapidity correlations changes with colliding energy, the ridge yields  $Y$  at  $\sqrt{s} = 5.02$  TeV and 8.16 TeV are presented in Fig. 1(b). The red curve (representing 5.02 TeV) nearly coincides with the black dotted line (representing 8.16 TeV) for  $|\Delta y| < 2$ , but deviates significantly for  $|\Delta y| > 2$ . The red curve (for 5.02 TeV) donates a noticeable rebound at  $|\Delta y| \approx 3.5$  after a plateau within  $2 < |\Delta y| < 3.5$ . In contrast, the black dotted line (for 8.16 TeV) falls first then rebounds at  $|\Delta y| \approx 3.8$ . The positions of correlation rebound at two energies are different. Figure. 1(b) indeed shows the rebound of large-rapidity ridge correlations shifts to larger rapidity gap at higher collision energies. This occurs because the rapidity  $y$  increases with  $\sqrt{s}$  at fixed  $x$  and  $p_T$ , as shown in Eq. (1). Gluons with larger rapidity represent source gluons. The rebound of rapidity correlations at  $|\Delta y| \approx 4.0$  is caused by the strong correlations between the radiated gluons and source gluons. As Eq. (1) demonstrates, the rapidity  $y_q$  increases with  $\sqrt{s}$  to get the same  $x$ . As a result, the rapidity gap  $\Delta y$  ( $\Delta y = y_q - y_p$ ) must increase with  $y_q$  when  $y_p$  is fixed.

#### IV. TRANSVERSE MOMENTUM DEPENDENCE OF LONG-RANGE RAPIDITY CORRELATIONS

According to Eq. (1),  $x$  is proportional to the transverse momentum  $p_T$  at fixed  $y$  and  $\sqrt{s}$ . The transverse momentum can also affect the correlation rebound. In the following, it is interesting to see how the rebound of large-rapidity correlations changes with the transverse momentum for the rapidity window of  $[-2.4, 2.4]$  at  $\sqrt{s} =$

5.02 TeV in p-Pb collisions. In order to systematically study the transverse momentum dependence, the transverse momenta of two particles are set to identical and different intervals, respectively. The results are shown in Fig. 2. The rapidity correlations within  $p_T(q_T) \in [1, 2]$  GeV/c (the red curve in Fig. 2(a)) completely reproduce the trend of the red curve for  $p_T(q_T) \in [1, 3]$  GeV/c in Fig. 1(b). The rebound of the red curve at  $|\Delta y| \approx 3.5$  in Fig. 1(b) is dominated by the transverse momentum interval  $[1, 2]$  GeV/c. The correlations at  $p_T(q_T) \in [2, 3]$  GeV/c (the black dotted line in Fig. 2(a)) do not show any rebound trends. It indicates that the rebound of rapidity correlations at  $|\Delta y| \approx 3.5$  is most obvious at  $p_T(q_T) \sim Q_{sA} + Q_{sB} \approx 2$  GeV/c, where  $Q_{sA(B)}$  denotes the saturation momentum of the projectile (A) or target (B). As we know, the only parameter in the CGC framework is the saturation momentum  $Q_s$ , which is  $\sqrt{s}$  dependent. At 5.02 TeV, the saturation momentum of proton and lead nucleus are  $Q_{sp} \approx 0.8$  GeV/c and  $Q_{sA} \approx 1.2$  GeV/c (see Fig. 2(a) in Ref. [66]). This is consistent with the existing experimental result that ridge yield gets the maximum within  $[1, 2]$  GeV/c of particle transverse momentum [2]. For this reason, we always choose  $p_T \in [1, 2]$  GeV/c in the following.

As Fig. 2(b) shows, the ridge yield  $Y$  at  $q_T \in [2, 4]$  GeV/c falls first and then rises with  $|\Delta y|$ , showing a visible rebound after the plateau in the rapidity direction. A striking difference from Fig. 2(a) is that the rapidity correlations become asymmetric. The correlation rebound at  $\Delta y \approx -3.5$  is higher and more obvious than at  $\Delta y \approx 3.5$ , indicating a stronger correlation at  $\Delta y \approx -3.5$ . It is further observed that the distribution of  $Y(\Delta y)$  reverses when the  $p_T$  and  $q_T$  intervals are swapped, i.e.,

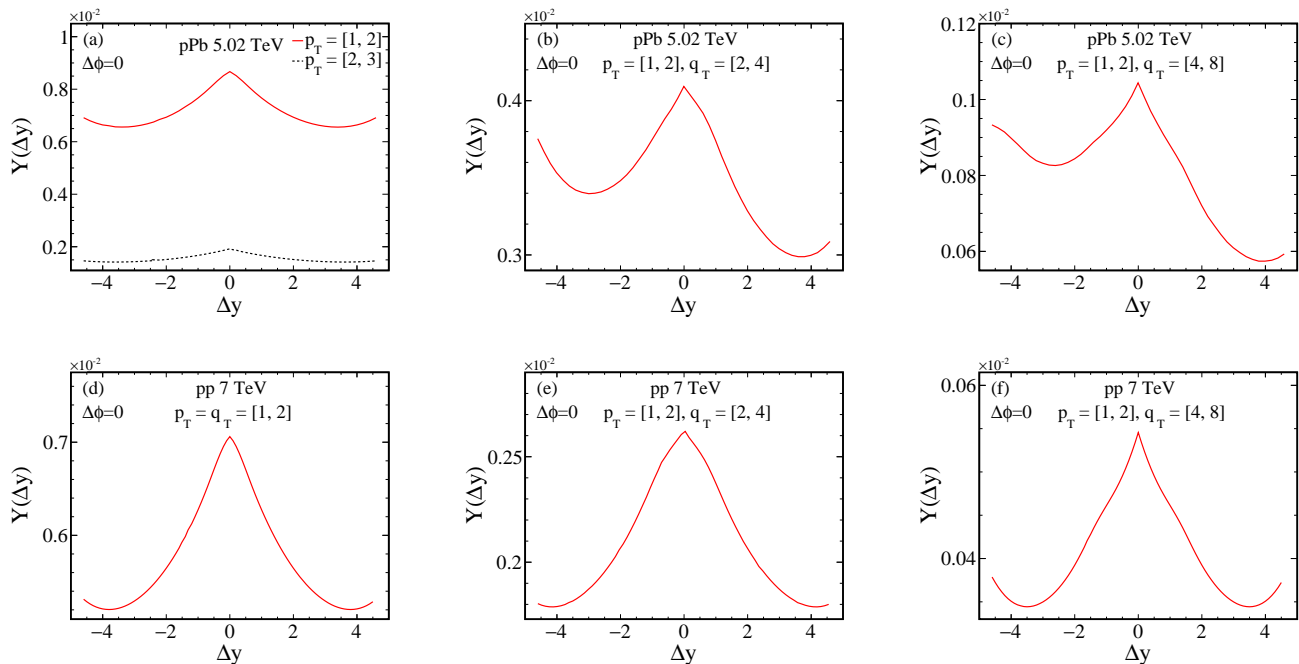


FIG. 2: The near-side per-trigger yield as a function of  $\Delta y$  at 5.02 TeV p-Pb collisions (top row) and 7 TeV pp collisions (bottom row) within the rapidity windows  $[-2.4, 2.4]$ , (a) the red curve and black dotted line represent the ridge yield in transverse momentum interval  $p_T(q_T) \in [1, 2]$  and  $[2, 3]$  GeV/c, respectively, the ridge yield for transverse momentum interval  $p_T \in [1, 2]$  GeV/c,  $q_T \in [2, 4]$  GeV/c (b), for  $p_T \in [1, 2]$  GeV/c,  $q_T \in [4, 8]$  GeV/c (c), for  $p_T(q_T) \in [1, 2]$  GeV (d), for  $p_T \in [1, 2]$  GeV/c,  $q_T \in [2, 4]$  GeV/c (e) and for  $p_T \in [1, 2]$  GeV/c,  $q_T \in [4, 8]$  GeV/c (f), respectively.

$p_T \in [2, 4]$  GeV/c and  $q_T \in [1, 2]$  GeV/c. In this case, the correlation rebound at  $\Delta y \approx -3.5$  is lower and less pronounced than  $\Delta y \approx 3.5$ . A stronger correlation appears at  $\Delta y \approx 3.5$  instead of  $\Delta y \approx -3.5$ .

The rapidity correlations at  $q_T \in [4, 8]$  GeV/c are illustrated in Fig. 2(c). The curve in Fig. 2(c) is similar to the curve in Fig. 2(b), with the exception of the amplitude. As Fig. 2(c) shows, a rebound occurs at  $|\Delta y| \approx 3.5$  after the plateau within  $2 < |\Delta y| < 3.5$ . The correlation rebound at  $\Delta y \approx -3.5$  is stronger and more distinct than at  $\Delta y \approx 3.5$ .

Comparing Figs. 2(a), 2(b) and 2(c), we observe that the amplitude of  $Y(\Delta y)$  decreases as  $q_T$  increases. The rapidity correlations are asymmetric in p-Pb collisions at different  $p_T$  and  $q_T$  intervals, but become symmetric when the intervals of  $p_T$  and  $q_T$  overlap.

To verify whether the asymmetric rapidity correlations are unique to p-Pb collisions in the CGC framework, the rapidity correlations for pp collisions at 7 TeV within rapidity window  $[-2.4, 2.4]$  are calculated for comparison. The rapidity correlations for pp collisions with  $p_T(q_T) \in [1, 2]$  GeV/c are shown in Fig. 2(d). For  $q_T \in [2, 4]$  GeV/c and  $[4, 8]$  GeV/c ( $p_T \in [1, 2]$  GeV/c), the correlations are illustrated in Figs. 2(e), 2(f), respectively. As Figs. 2(d), 2(e) and 2(f) show, all three curves have similar structures. They first fall and then rise with  $|\Delta y|$ , showing a rebound after the plateau in the rapidity direction. Additionally, the amplitude of  $Y(\Delta y)$  decreases

as  $q_T$  increases. In contrast to p-Pb collisions, the rapidity correlations in pp collisions are always symmetric, regardless of the variations in the transverse momenta of two particles.

Comparing with Figs. 2, a unique finding is that the rapidity correlations in p-Pb collisions demonstrate asymmetry when the transverse momenta of two particles are different.

These transverse momentum dependencies of the large-rapidity ridge correlations can be well explained within the CGC framework. The correlation function is proportional to the correlated two-gluon production, i.e., Eq. (7), which can be expressed by convolutions of four uGDs [31–33, 66, 68, 69], e.g.,

$$\Phi_A^2(y_p, \mathbf{k}_T) \Phi_B(y_p, \mathbf{p}_T - \mathbf{k}_T) \Phi_B(y_q, \mathbf{q}_T - \mathbf{k}_T). \quad (16)$$

The uGD ( $\Phi$ ) peaks at  $Q_s$ , transverse momentum far from  $Q_s$  contributes little to the correlation. The strongest correlation [29, 66, 68] requires simultaneously,

$$|\mathbf{k}_T| \sim Q_{sp}, \quad |\mathbf{p}_T - \mathbf{k}_T| \sim Q_{sA} \quad \text{and} \quad |\mathbf{q}_T - \mathbf{k}_T| \sim Q_{sA}. \quad (17)$$

In the context, the maximum of the correlation should be near  $|\mathbf{p}_T| \sim |\mathbf{q}_T| \sim Q_{sp} + Q_{sA} \sim 2$  GeV/c in pA collisions. As  $q_T$  increases and moves farther from  $Q_s$ , the correlation becomes weaker. Therefore, the amplitude of  $Y(\Delta y)$  in Figs. 2 decreases with  $q_T$  increases.

Last but not least, let's clarify the reasons for the

TABLE I: An example of the Bjorken  $x$  values at  $|\Delta y| = 3.5$  in symmetric and asymmetric rapidity windows.

Acceptance	$Y_w = [-2.4, 2.4]$		$Y_w = [-2.865, 1.935]$	
Rapidity gap	$\Delta y = -3.5$	$\Delta y = 3.5$	$\Delta y = -3.5$	$\Delta y = 3.5$
$x$ -values	$x_q = \frac{q_T}{\sqrt{s}} e^{2.0}$ $x_p = \frac{p_T}{\sqrt{s}} e^{1.5}$	$x_q = \frac{q_T}{\sqrt{s}} e^{2.0}$ $x_p = \frac{p_T}{\sqrt{s}} e^{1.5}$	$x_q = \frac{q_T}{\sqrt{s}} e^{2.4}$ $x_p = \frac{p_T}{\sqrt{s}} e^{1.0}$	$x_q = \frac{q_T}{\sqrt{s}} e^{1.0}$ $x_p = \frac{p_T}{\sqrt{s}} e^{2.4}$

formation of asymmetric rapidity correlations. As mentioned earlier, the gluon at different rapidity regions reflects different stages of gluon evolution. Large-rapidity ridge correlations reflect strong correlations between source gluons and radiated gluons. In a symmetric rapidity window, like the CMS acceptance  $[-2.4, 2.4]$ , the rapidity of two particles can take opposite values at same  $|\Delta y|$ , e.g.,  $y_q = -2(2)$  and  $y_p = 1.5(-1.5)$  for  $\Delta y = -3.5(3.5)$ . According to Table. 1,  $x_q, x_p$  at  $|\Delta y|=3.5$  respectively correspond to equality. It means that the correlations are always identical at same  $|\Delta y|$ . Thus, in symmetric collision systems, such as pp and AA collisions, the rapidity correlations are symmetric.

In asymmetric collision systems, like pA collisions, the asymmetry of the colliding nucleus leads to different rapidity windows in the laboratory and center-of-mass frames. For instance, the CMS acceptance is  $[-2.4, 2.4]$  in laboratory frame, but is  $[-2.865, 1.935]$  in center-of-mass frame. Theoretical calculations carry out in the center-of-mass frame, so the rapidity window is  $[-2.865, 1.935]$  in our calculation. At large-rapidity gap  $|\Delta y|$ , the rapidity of two particles can only swap magnitudes, not signs, e.g.,  $y_q = -2.4(1.0)$  and  $y_p = 1.0(-2.4)$  for  $\Delta y = -3.5(3.5)$ . As shown in Table. 1, although  $x_q, x_p$  are different at  $|\Delta y|=3.5$ ,  $|x_q - x_p|$  are the same when  $p_T$  and  $q_T$  are identical. It means that  $|x_q - x_p|$  are always identical at same  $|\Delta y|$  when the transverse momentum intervals of two particles coincide. The correlation patterns are dependent on the  $x$ -component of two selected gluon. Therefore, the rapidity correlations are identical at same  $|\Delta y|$  and are symmetric shown in Fig. 2(a).

When  $p_T$  and  $q_T$  are unequal,  $x_q, x_p$  at  $|\Delta y|=3.5$  are different, and so do  $|x_q - x_p|$  and correlation strength. We can find  $x_q = 0.0022$  and  $x_p = 0.0047$  at  $\Delta y = 3.5$ ,  $x_q = 0.0094$  and  $x_p = 0.0011$  at  $\Delta y = -3.5$  for  $p_T = 2$  and  $q_T = 4$ . At  $\Delta y = -3.5$ ,  $x_q$  is closer the large  $x(x > 0.01)$ , leading to the formation of a quasi large- $x$  and small- $x$  correlation pair. Consequently, the correlations at  $\Delta y = -3.5$  are stronger than those at  $\Delta y = 3.5$ . Moreover,  $y_q$  decreases with  $\Delta y$  at  $\Delta y < -3.5$ ,  $x_q$  increases with  $\Delta y$  decreases and is closer the large  $x(x > 0.01)$ . As a result, the correlation rebound becomes more significant at  $\Delta y < -3.5$ , as shown in Fig. 2(b) and 2(c). When the intervals of  $p_T$  and  $q_T$  are swapped, i.e.,  $p_T \in [2, 4]$  and  $q_T \in [1, 2]$ , then  $|x_q - x_p|$  at  $\Delta y = 3.5$  is larger than at  $\Delta y = -3.5$ . This causes the distribution of  $Y(\Delta y)$  to reverse. In this manuscript, we calculated that the lead nucleus along the beam direction collide with proton, swapping the proton and lead nucleus will reverse the

correlation pattern.

The asymmetry in rapidity correlations originates from the inherent asymmetry of the colliding hadron or nucleus in rapidity. The asymmetric rapidity window in the center-of-mass frame causes an asymmetric selections for particle pairs with the same  $|\Delta y|$ , resulting in different  $x$  values and correlation strength at same  $|\Delta y|$ . This ultimately creates the asymmetric rapidity correlations. The patterns of long-range rapidity correlations with respect to  $p_T$  and  $\sqrt{s}$  are a characteristic of the CGC mechanism. Identifying these characteristics is a possible way to test the mechanism of the CGC.

## V. SUMMARY AND DISCUSSIONS

Within the framework of CGC, we study the long-range rapidity correlations in p-Pb collisions at  $\sqrt{s_{NN}} = 5.02$  TeV by using the exact normalization scheme proposed in our previous paper [70]. After this normalization, the ridge correlation at large rapidity rebounds after bottoming, which is successfully described by the CGC.

The correlation rebound at large rapidity separation is found to appear around the sum of the saturation momentum of the projectile and target. This feature is directly caused by the effect of gluon saturation in the theory of CGC. Meanwhile, the rebound moves to larger rapidities at higher colliding energies.

It is further found that the near-side rapidity correlations are asymmetric in p-Pb collisions when the transverse momenta of two particles are different. The asymmetry in rapidity correlations arises from the inherent asymmetry of the colliding hadron or nucleus in rapidity. The asymmetric rapidity window and the different transverse momenta of two particles jointly result in the asymmetric rapidity correlations. The rapidity as well as transverse momentum can affect the Bjorken  $x$ . Correlations of gluons of different  $x$  essentially reflect correlations of different generations. So the asymmetry in rapidity correlations are sensitive to the quantum evolution of gluon within the CGC framework.

The physics of different rapidity regions reflect different stages of gluon evolution in the CGC framework. The correlation patterns are dependent on the  $x$ -component of two selected gluons. This physical picture may also understand the ridge correlations of two particles at different rapidity regions in pA collisions given by ALICE collaborations [75].

The rebound structure at large rapidity separation

and the asymmetric ridge correlation are caused by the stronger correlation between source gluons and radiated gluons. These features are independent of the speed of the small  $x$  evolution and the selection of initial conditions. Therefore, the selection of running coupling kernels and initial conditions does not influence the qualitative feature of the results.

So far the correlation patterns calculated are for gluons. The fragmentation functions reflecting final hadronization should also be considered. As Ref. [30] shows, including fragmentation functions brings integrations over  $z$ , the transverse momentum fraction of the produced hadron with respect to that of the fragmenting gluon, the rapidity correlations of two hadrons at a certain transverse momentum, e.g.,  $p_0$ , take into account the contributions of all gluons with transverse momenta larger than  $p_0$ . Therefore fragmentation functions only have a major impact on transverse momentum dependence. The correlation patterns are dependent on the  $x$ -component of two selected gluon. According to Eq. (1), the influence of transverse momentum on Bjorken  $x$  is much smaller than that of rapidity. This should not change qualitatively the rebound features at parton level. From the results, the rebound structures are still prominent and rapidity correlations  $Y(\Delta y)$  are always asymmetric even the increase of  $q_T$  in Figs. 2. Therefore the correlation patterns as a function of rapidities would remain in the final state. Besides, the nonperturbative effects specifying the correction to the  $k_T$  factorized uGD description is regarded as constant [34].

In this manuscript, only glasma graph is calculated which results in both the near-side and the away-side ridge, i.e., the so-called double ridges. Other effects also give significant contributions to the two-particle correlations, e.g. Mueller-Navelet di-jet and jet shower effects. It is known that di-jet mainly contributes to the away-side ridge and jet shower contributes to short-range correlations of the near side. When long-range rapidity correlations of the near side are considered, both effects are negligible. Further observation the rebound of large-rapidity ridge correlation and the asymmetry in rapidity correlations in experiments is a direct test of the CGC mechanism, and therefore is very meaningful and interesting.

### Acknowledgement

This research was partially supported by the National Key Research and Development Program of China, grant number 2022YFA1604900; the National Natural Science Foundation of China, grant number 12275102; the Fundamental Research Funds of China West Normal University, grant number 22kE042; the Scientific Research and Innovation Team Program of Sichuan University of Science and Engineering(No.SUSE652A001). The numerical simulations have been performed on the GPU cluster in the Nuclear Science Computing Center at Central China Normal University (NSC3).

- 
- [1] The ATLAS Collab., Phys. Rev. C **104**, 014903 (2021).
  - [2] The CMS Collab., J. High Energy Phys. **09**, 091 (2010).
  - [3] D. Velicanu (for the CMS Collab.), J. Phys. G **38**, 124051 (2011).
  - [4] The ATLAS Collab., ATLAS NOTE, Report No. ATLAS-CONF-2015-027.
  - [5] The CMS Collab., Phys. Rev. Lett. **116**, 172302 (2016).
  - [6] The ALICE Collab., Eur. Phys. J. C **77**, 569 (2017).
  - [7] The CMS Collab., Phys. Lett. B **765**, 193 (2017).
  - [8] The CMS Collab., Phys. Lett. B **718**, 795 (2013).
  - [9] The ALICE Collab., Phys. Lett. B **719**, 29 (2013).
  - [10] The ATLAS Collab., Phys. Rev. Lett. **110**, 182302 (2013).
  - [11] The ATLAS Collab., Phys. Lett. B **725**, 60 (2013).
  - [12] The CMS Collab., Phys. Lett. B **724**, 213 (2013).
  - [13] The ALICE Collab., Phys. Lett. B **753**, 126 (2016).
  - [14] The CMS Collab., CMS Physics Analysis Summary, Report No. CMS PAS HIN-11-006.
  - [15] The CMS Collab., J. High Energy Phys. **07**, 076 (2011).
  - [16] The CMS Collab., Eur. Phys. J. C **72**, 2012 (2012).
  - [17] The PHENIX Collab., Phys. Rev. C **78**, 014901 (2008).
  - [18] The STAR Collab., Phys. Rev. C **80**, 064912 (2009).
  - [19] The PHOBOS Collab., Phys. Rev. Lett. **104**, 062301 (2010).
  - [20] P. Romatschke, U. Romatschke, Phys. Rev. Lett. **99**, 172301 (2007).
  - [21] H. Song, U. Heinz, Phys. Lett. B **658** (2008) 279.
  - [22] B. Schenke, S. Jeon, C. Gale, Phys. Rev. Lett. **106** (2011) 042301.
  - [23] F.G. Gardim, F. Grassi, M. Luzum, J.Y. Ollitrault, Phys. Rev. Lett. **109** (2012) 202302.
  - [24] C. Gale, S. Jeon, B. Schenke, P. Tribedy, R. Venugopalan, Phys. Rev. Lett. **110** (2013) 012302.
  - [25] L. He, T. Edmonds, Z.W. Lin, F. Liu, D. Molnar, F. Wang, Phys. Lett. B **753** (2016) 506.
  - [26] H. Song, Y. Zhou, K. Gajdosova, Nucl. Sci. Tech. **28** (2017) 99.
  - [27] A. Dumitru, F. Gelis, L. McLerran, R. Venugopalan, Nucl. Phys. A **810**, 91 (2008).
  - [28] K. Dusling, F. Gelis, T. Lappi, R. Venugopalan, Nucl. Phys. A **836**, 159 (2010).
  - [29] A. Dumitru, K. Dusling, F. Gelis, J. Jalilian-Marian, T. Lappi, R. Venugopalan, Phys. Lett. B **697**, 21 (2011).
  - [30] K. Dusling, R. Venugopalan, Phys. Rev. Lett. **108**, 262001 (2012).
  - [31] K. Dusling and R. Venugopalan, Phys. Rev. D **87**, 051502(R) (2013).
  - [32] K. Dusling and R. Venugopalan, Phys. Rev. D **87**, 054014 (2013).
  - [33] K. Dusling and R. Venugopalan, Phys. Rev. D **87**, 094034 (2013).
  - [34] M Mace, V. V. Skokov, P. Tribedy, R. Venugopalan, Phys. Lett. B **788**, 161 (2019).
  - [35] Y. Shi, L. Wang, S. Wei, B. Xiao, L. Zheng, Phys. Rev.



- D **103**, 054017 (2021).
- [36] K. Werner, Iu. Karpenko, T. Pierog, Phys. Rev. Lett. **106**, 122004 (2011).
- [37] P. Bozek, W. Broniowski, Phys. Lett. B **718**, 1557 (2013).
- [38] A. Bzdak, B. Schenke, P. Tribedy, R. Venugopalan, Phys. Rev. C **87**, 064906 (2013).
- [39] G. Qin and B. Muller, Phys. Rev. C **89**, 044902 (2014).
- [40] K. Werner, M. Bleicher, B. Guiot, Iu. Karpenko, T. Pierog, Phys. Rev. Lett. **112**, 232301 (2014).
- [41] Ryan D. Weller a, Paul Romatschke, Phys. Lett. B **774**, 351–356 (2017).
- [42] J. L. Nagle and W. A. Zajc, Ann. Rev. Nucl. Part. Sci. **68**, 211 (2018).
- [43] W. Zhao, Y. Zhou, H. Xu, W. Deng, H. Song, Phys. Lett. B **780**, 495 (2018).
- [44] The ALICE Collab., Phys. Lett. B **726**, 164 (2016).
- [45] The CMS Collab., Phys. Lett. B **742**, 200 (2015).
- [46] The ALICE Collab., Phys. Lett. B **728**, 25 (2014).
- [47] The ALICE Collab., Phys. Rev. Lett. **110**, 082302 (2013).
- [48] The ALICE Collab., Phys. Lett. B **760**, 720 (2016).
- [49] B. Schenke, S. Schlichting, P. Tribedy, R. Venugopalan, Phys. Rev. Lett. **117**, 162301 (2016).
- [50] K. Dusling, M. Mace, R. Venugopalan, Phys. Rev. Lett. **120**, 042002 (2018).
- [51] M. Mace, V. V. Skokov, P. Tribedy, R. Venugopalan, Phys. Rev. Lett. **123**, 039901 (2019).
- [52] The ALICE Collab., Phys. Lett. B **780**, 7 (2018).
- [53] The CMS Collab., Report No. CMS-PAS-HIN-18-010.
- [54] The CMS Collab., Phys. Rev. Lett. **121**, 082301 (2018).
- [55] The CMS Collab., CMS-PAS-HIN-19-009.
- [56] C. Zhang, C. Marquet, G. Qin, S. Wei, B. Xiao, Phys. Rev. Lett. **122**, 172302 (2019).
- [57] X. Du, R. Rapp, J. High Energy Phys. **03**, 015 (2019).
- [58] G. Giacalone, B. Schenke, C. Shen, Phys. Rev. Lett. **125**, 192301 (2020).
- [59] S. H. Lim, J. L. Nagle, Phys. Rev. C **103**, 064906 (2021).
- [60] Y. Kanakubo, Y. Tachibana and T. Hirano, Phys. Rev. C **105**, 024905 (2022).
- [61] E. Iancu, R. Venugopalan, arXiv:hep-ph/0303204.
- [62] I. Balitsky, Nucl. Phys. B **463**, 99 (1996).
- [63] Y.V. Kovchegov, Phys. Rev. D **60**, 034008 (1999).
- [64] J. L. Albacete, Y. V. Kovchegov, Phys. Rev. D **75**, 125021 (2007).
- [65] N. Armesto, L. McLerran, C. Pajares, Nucl. Phys. A **781**, 201 (2007).
- [66] Yeyin Zhao, Mingmei Xu, Hengying Zhang and Yuanfang Wu, Nucl. Phys. A **955**, 88 (2016).
- [67] Yeyin Zhao, Mingmei Xu, Hengying Zhang, Yuanfang Wu, arXiv:1709.08678.
- [68] Hengying Zhang, Donghai Zhang, Yeyin Zhao, Mingmei Xu, Xue Pan and Yuanfang Wu, Phys. Rev. D **97**, 034003 (2018).
- [69] Donghai Zhang, Yeyin Zhao, Mingmei Xu, Xue Pan and Yuanfang Wu, Nucl. Phys. A **1011**, 122201 (2021).
- [70] Donghai Zhang, Yeyin Zhao, Mingmei Xu, Yuanfang Wu, Phys. Rev. D **107**, 056017(2023).
- [71] M. Gazdzicki, M. I. Gorenstein and M. Mackowiak-Pawlowska, Phys. Rev. C **88**, 024907 (2013).
- [72] J. L. Albacete, N. Armesto, J. G. Milhano, P. Quiroga Arias, and C. A. Salgado, Eur. Phys. J. C **71**, 1705 (2011).
- [73] I. Balitsky, Phys. Rev. D **75**, 014001 (2007).
- [74] J. L. Albacete and A. Dumitru, arXiv:1011.5161.
- [75] The ALICE Collab., J. High Energy Phys. **01**, 199 (2024).